

# FootNet v1.0: Development of a machine learning emulator of atmospheric transport

Tai-Long He<sup>1,a,\*</sup>, Nikhil Dadheech<sup>1,\*</sup>, Tammy M. Thompson<sup>2</sup>, and Alexander J. Turner<sup>1</sup>

<sup>1</sup>Department of Atmospheric and Climate Science, University of Washington, Seattle, WA, USA

<sup>2</sup>Environmental Defense Fund, Boulder, CO, USA

<sup>a</sup>now at: School of Engineering and Applied Sciences, Harvard University, Cambridge, 02138, USA

\*These authors contributed equally to this work.

**Correspondence:** Alexander J. Turner (turneraj@uw.edu)

**Abstract.** There has been a proliferation of dense observing systems to monitor greenhouse gas (GHG) concentrations over the past decade. Estimating emissions with these observations is often done using an atmospheric transport model to characterize the source-receptor relationship, which is commonly termed measurement “footprint”. Computing and storing footprints using full-physics models is becoming expensive due to the requirement of simulating atmospheric transport at high resolution.

5 We present the development of FootNet, a deep learning emulator of footprints at kilometer scale. We train and evaluate the emulator using footprints simulated using a Lagrangian particle dispersion model (LPDM). FootNet predicts the magnitudes and extents of footprints in near real-time with high fidelity. We identify the relative importance of input variables of FootNet to improve the interpretability of the model. Surface winds and a precomputed Gaussian plume from the receptor are identified to be the most important variables for footprint emulation. The FootNet emulator developed here may help address the  
10 computational bottleneck of flux inversions using dense observations.

## 1 Introduction

Monitoring anthropogenic greenhouse gas (GHG) emissions is important for ensuring the success of the Paris Agreement’s long-term goal on mitigating climate change (IPCC, 2022). To that end, there has been a proliferation of dense observing systems over the past decade to better track GHG emissions. Substantial efforts have been made to expand observation networks  
15 to better quantify urban GHG emissions, as the majority of the world population lives in urban areas and the degree of urbanization is projected to increase in the future (United Nations Publications, 2019). For example, the Northeast Corridor GHG observation network was established to quantify emissions of carbon dioxide and methane using tower-based *in situ* measurements in urban regions in the northeastern United States (Karion et al., 2020). The Berkeley Atmospheric CO<sub>2</sub> Observation Network (BEACO<sub>2</sub>N; Shusterman et al., 2016) utilizes low-cost sensors to increase the spatial density of measurements, which  
20 could be used to estimate urban emissions on intra-city scales in the San Francisco (SF) Bay Area. The proliferation of urban GHG observation networks allows for decadal analyses of GHG emissions and provides information to improve the efficiency of GHG reduction policies (Mitchell et al., 2018; Lauvaux et al., 2020). There has been a coincident expansion in space-borne GHG monitoring instruments, which provide similarly dense observations, such as NASA’s Orbiting Carbon Observatory-2

(OCO-2) and OCO-3, the TROPOspheric Monitoring Instrument (TROPOMI) onboard the Copernicus Sentinel-5 Precursor (S5P) satellite (Veefkind et al., 2012), MethaneSat for methane, and a planned constellation of GHG monitoring satellites (e.g., GOSAT-GW).

The increased volume of observational data sets provide more constraints to estimate GHG emissions. However, current methods do not scale well with the increasing number of observations. Inferring GHG emissions using atmospheric observations is conventionally done via atmospheric flux inversions (e.g., Jiang et al., 2017; White et al., 2019; Turner et al., 2020). The state of the art in atmospheric flux inversions relies on either Eulerian models or Lagrangian particle dispersion models (LPDMs) to simulate atmospheric transport, which provides the means of relating observations to surface fluxes. For example, the four-dimensional variational (4D-Var) method uses the adjoint of Eulerian models to calculate sensitivities of GHG concentrations to surface fluxes (Baker et al., 2006; Henze et al., 2007; Jiang et al., 2017; Qu et al., 2022). Kalman filters are also widely used in flux inversions, which calculate covariance matrices between prior fluxes and GHG concentrations simulated by Eulerian models to estimate posterior fluxes (Feng et al., 2009; Kang et al., 2011; Miyazaki et al., 2017, 2020). Alternatively, LPDMs can be used to calculate the sensitivity of each observation to its upwind sources by simulating the trajectories of an ensemble of particles advected backward in time (Lin et al., 2004; Fasoli et al., 2018; Jones et al., 2007b; Pisso et al., 2019). The sensitivity of each receptor to its upwind sources, termed as the receptor’s “footprint”, can then be used to estimate fluxes inversely (e.g., Stohl et al., 2003, 2009; Jones et al., 2007a; Lin et al., 2004, 2021; Stein et al., 2015; Turner et al., 2020). These methods based on full-physics models are becoming prohibitively expensive due to the large computational burden of running high-resolution atmospheric transport models for dense observing systems. The 4D-Var method runs the forward and adjoint models iteratively to optimize the a posteriori emission, which is hard to parallelize. Kalman filters could benefit from parallelism, however, they still require the forward model and the computational cost scales up with the number of processors used (e.g., Houtekamer and Mitchell, 2001).

Here we present a machine learning-based emulator, FootNet, to efficiently calculate footprints of ground-based receptors with a high fidelity at kilometer-scale spatial resolution. The footprint emulator reduces the computational and storage cost of Lagrangian model-based flux inversion systems by 2–3 orders of magnitude, which will better accommodate the increased volume of GHG observations. We show the evaluation of the performance of FootNet using independent data sets. Finally, we assess the relative importance of the input variables of FootNet using the permute-and-prediction (PaP) method.

## 2 Construction of the FootNet emulator

Training of the FootNet model is a supervised learning process, which requires ground truth to guide the optimization of the model parameters. Here, we use a full-physics model to generate the ground truth. We simulate footprints using the Stochastic Time-Inverted Lagrangian Transport (STILT) model (Lin et al., 2003; Fasoli et al., 2018), a Lagrangian particle dispersion model (LPDM). STILT simulations are conducted for two regions: the Barnett Shale region in Texas, and the SF Bay Area in California (see Figure 2). These two regions are chosen because one has simple topography (the Barnett Shale) whereas the other is topographically complex (SF Bay Area). As such, these regions represent limiting cases for the construction and

evaluation of the emulator. Further, the combination of two regions will help prevent from overfitting the model to a single location. For the SF Bay Area, STILT simulations are run from 2018 to 2020 with receptors located at realistic sites deployed in the BEACO<sub>2</sub>N network (see <http://beacon.berkeley.edu> and Shusterman et al. (2016)). Footprints for the Barnett Shale region are generated from a 1-week WRF-STILT simulation in 2013 (Turner et al., 2018). All STILT runs are conducted within 400×400 km<sup>2</sup> domains at 1×1 km<sup>2</sup> spatial resolution (see Figure 1). The footprints are integrated 72 hours backwards from the measurement time, because of the 400 km × 400 km domain used by the FootNet model. The time integration period could change depending on the spatial and time scales of inversion systems.

The output of FootNet is a source-receptor relationship (i.e., footprint, **H**), which represents the sensitivity of atmospheric concentrations at a receptor site to emissions upwind of the receptor. This relationship between the measured concentrations and the emissions in the upwind area can be formulated as

$$\mathbf{y} = \mathbf{H}\mathbf{x} + \mathbf{b}$$

where **y** represents the measured concentration, **x** is the emission fluxes in a domain around the measurement location, and **b** is the background concentration upwind of the domain. The units of **y** and **x** can be expressed as dry air mixing ratio (ppb) and flux rates (nmol m<sup>-2</sup> s<sup>-1</sup>), respectively (Lin et al., 2003). The source-receptor relationships, **H** = ∂**y**/∂**x**, therefore have units of ppb / (nmol m<sup>-2</sup> s<sup>-1</sup>).

The calculation of measurement footprints is independent of the observed gas concentrations and could be constructed using meteorological variables only. As shown in Table 1, we use 4 physical parameters from the NOAA High-Resolution Rapid Refresh (HRRR; Benjamin et al. (2016)) model as the input variables, including the 10-meter zonal wind speed (U10M), 10-meter meridional wind speed (V10M), planetary boundary layer height (PBLH) and surface pressure (PRSS). The FootNet model receives input variables at the measurement time (*t*<sub>0</sub>) and 6 hours before the measurement time (*t*<sub>0</sub>-6h) to predict footprints at *t*<sub>0</sub>. The choice of 6 hours backwards was determined by a series of sensitivity tests on the amount of history information in the input data (see Supplemental Section S1). We found that including history information from more than 6 hours could not further improve the performance of FootNet in the emulation (see Figures S1-3). However, we note that the results from the sensitivity tests could depend on the spatial and temporal scale and resolution of the specific inversion problems. Evaluation of the necessary history information in other spatio-temporal regions is warranted.

We scale the input variables to a similar magnitude for the stabilization of the training process (see Table 1). The output of FootNet is measurement footprints and is transformed by the natural logarithm function to reduce the skewness of the distribution of footprint values. The transformed footprints are filtered to remove values smaller than -20 and then shifted by +20, corresponding to a scaling of the raw footprints by  $e^{20}$ . We find that including Gaussian plumes (see Figure 1) as one of the input variables could significantly improve the performance of FootNet. The Gaussian plumes are calculated using the Gaussian plume model (e.g., Stern, 1976; Dobbins, 1979; Zannetti, 1990, among others) with reversed wind fields starting from the measurement site, which are used as the initial guess of the upwind areas and the measurement footprints. The Gaussian plumes can be efficiently calculated as a Hadamard product from inputs listed above and, as such, adds minimal computational expense. The Gaussian plumes also provide a localization for FootNet in that it contains the information about measurement

location and provides an initial guess for the spatial structure of the footprint. The FootNet model is trained to learn the nonlinear transformation from the idealized Gaussian plumes to measurement footprints using the meteorological fields. The input variables are interpolated to the  $400 \times 400 \text{ km}^2$  domain and the  $1 \times 1 \text{ km}^2$  spatial resolution of footprints.

90 The model structure underlying the footprint emulator is the U-net model (Ronneberger et al., 2015), which is now broadly applied in the field of Earth Science (Ghorbanzadeh et al., 2021; He et al., 2022a, b; Zemsanova et al., 2022; Tucker et al., 2023; He et al., 2024). A schematic diagram of the model architecture is shown in Figure 1. The model consists of 4 convolutional blocks and 4 up-convolutional blocks. Each convolutional block is a sequence of two convolutional layers with  $3 \times 3$  kernels and one  $2 \times 2$  max-pooling layer. In each convolutional layer, the input images will be performed the convolution calculation  
 95 with  $3 \times 3$  kernels that will scan the whole images to generate output images. In max-pooling layers, the input images will be down-sampled by taking maximum values in each  $2 \times 2$  region in the images. Similarly, each up-convolutional layer has one  $2 \times 2$  up-convolutional layer followed by two  $3 \times 3$  convolutional layers. Up-convolutional layers perform transposed convolution operation with  $2 \times 2$  kernels scanning input images. The outputs from convolutional layers are all transformed by the Rectified Linear Unit (ReLU) function to increase non-linearity in predictions. In the training process, the entries of  $3 \times 3$   
 100 convolutional kernels and  $2 \times 2$  up-convolutional kernels will be optimized along the partial gradients of a loss function that measures the difference between the truth and FootNet predictions. More details about deep learning architectures could be found in Goodfellow et al. (2016).

We train and evaluate the emulator using a data set with 10,000 natural log-transformed footprints (logH) from the Barnett Shale and 10,000 footprints from the SF Bay Area as the truth. We apply natural logarithm transformation to the measurement  
 105 footprints because their values are often highly skewed, which could be challenging for the FootNet model to learn in the training process. The combined data set is randomly split to 85% as the training data set and 15% as the test data set. The test data set is independent of the training process. 15% of the training data set is used as a validation data set during the training process to prevent overfitting. We use mean squared error as the loss function and the Adam optimization algorithm.

We use the Intersection over Union (IoU) to measure the accuracy of the area of footprints predicted by FootNet, which is  
 110 defined as follows:

$$IoU = \frac{|Y \cap \hat{Y}|}{|Y \cup \hat{Y}|} \quad (1)$$

Here,  $Y$  and  $\hat{Y}$  stand for the ground truth (footprints simulated by STILT) and the FootNet predictions, respectively. The absolute value bars ( $|\cdot|$ ) here refer to the area of a region. Specifically, the intersection,  $|Y \cap \hat{Y}|$ , calculates the area of the region where both the truth and FootNet predictions show non-zero footprints. Similarly, the union,  $|Y \cup \hat{Y}|$ , represents the  
 115 area of the region where either the truth or FootNet predictions show non-zero footprints. IoU is widely used to evaluate the ability of deep learning models to make accurately localized predictions. We also compute Pearson correlation coefficients ( $r$ ) for footprints in the intersection areas between the truth, as simulated by STILT, and the corresponding FootNet predictions to help assess the performance.

Ultimately, we are interested in better understanding what drives the predictions from the FootNet model. As such, we use  
 120 the permute-and-prediction (PaP) method to calculate the importance of input variables for footprint emulation, which provides

some interpretability of the FootNet model (Fisher et al., 2019). The PaP method estimates variable importance by permuting each input variable with different data samples, and the subsequent performance change represents FootNet’s sensitivity to the permuted variable. We estimate variable importance by calculating performance changes in correlation, the IoU, and the root mean square error (RMSE) of the predicted footprints.

### 125 3 Evaluating performance of the FootNet emulator

Figure 3 demonstrates the evolution of FootNet predictions during the training process and the overall performance of FootNet after the training converges. Figure 3D shows a footprint simulated by the STILT model from the test data set, where the footprint is highly nonlinear with a change in direction near the receptor. The corresponding FootNet predictions are shown in Figures 3 (A-C). After iteration A (shortly after the training starts), the FootNet predicts measurement footprints around the  
130 receptor with a large negative bias and low correlation coefficient of 0.49. Iteration B is about halfway of the training process, after which the FootNet prediction better captures the general shape of the footprint and the correlation is improved to 0.61. The training stops after iteration C. The final FootNet prediction has enriched details and attains a correlation coefficient of 0.75. Compared to the truth in Figure 3D, the IoU of FootNet predictions improves from 0.28 after iteration A to 0.51 after iteration B, and attains a final IoU of 0.76 (see Figure 3E). Figure 3F shows the comparison between the truth and FootNet predictions  
135 for all footprints in the test data set. FootNet predictions show a slight negative bias compared to footprints simulated using the full-physics STILT model. The overall Pearson correlation coefficient ( $r$ ) between FootNet predictions and STILT simulations is 0.58. We conclude that FootNet is able to emulate the source-receptor relationship in both simple (Barnett Shale, TX) and complex (SF Bay Area, CA) meteorological conditions with high fidelity. However, it is worth mentioning here that we find some performance degradation using an alternative splitting of the data based on different time periods. Because the training data set used to construct version 1 of FootNet has a relatively small size, similarities between samples are hard to fully avoid by randomly selecting training data samples, which could lead to generalizability issues when using FootNet version 1 over regions and time periods too different from the training data set. This generalizability issue could be largely mitigated by increasing the volume of the training data set in the future (Dadheech et al., 2024).  
140

We then evaluate the performance of FootNet in predicting individual footprints for the two regions. Figure 4 shows foot-  
145 prints from STILT and FootNet for the two regions: the Barnett Shale and the SF Bay Area. Figures 4A and 4E show results from the simple case (Barnett Shale, TX), where the footprint is similar to an idealized Gaussian plume with time-reversed winds. FootNet well captures both the magnitudes and spatial patterns of the footprint, with an IoU of 0.73 and a correlation coefficient of 0.54. Figures 4B and 4F demonstrate a more complicated meteorological scenario in the Barnett Shale region. The IoU metric and correlation coefficient between the STILT footprint and the FootNet prediction are 0.71 and 0.61, respectively,  
150 for this more complex scenario.

Atmospheric transport in the SF Bay Area is decisively more complex because the region includes steep topography, air-sea interactions, and numerous valleys and deltas. Figures 4C and 4D show results from the full-physics model for the SF Bay Area. Emulation of footprints in the Bay Area is more challenging and with an overall degraded fidelity as compared to the

Barnett Shale region. Figures 4C and 4G show a receptor with the bulk of the footprint in the Northwest quadrant of the domain, as a result of typical summertime meteorology in the SF Bay Area with westerly flow bringing air masses into the SF Bay Area past the Golden Gate Bridge. The shape and the magnitude of the footprint is predicted by FootNet with an IoU of 0.53 and the correlation coefficient to be 0.83. Figures 4D and 4H show a more complex meteorological scenario, where the FootNet prediction has an IoU of 0.56 and the correlation is 0.78 as compared to STILT.

There have been other methods developed to improve the efficiency of footprint calculations. For example, Roten et al. (2021) uses nonlinear weighted averaging to interpolate footprints from locations near the receptors. Fillola et al. (2023) develops a similar footprint emulator based on gradient-boosted regression trees (GBRTs), at a coarse spatial resolution (20–30 km in mid-latitudes) and 10 grid cells around the measurement location. Compared to previous work, the FootNet model reproduces the full-physics model with high fidelity at high-resolution. This is remarkable given the complex topography and meteorology of the regions studied here could complicate transport at kilometer scale and the emulation of footprints. Moreover, FootNet only takes meteorological fields and the idealized Gaussian plume as its input. No additional LPDM simulations are needed to generate footprint predictions after the training process.

Emulation of footprints using the FootNet model brings co-benefits for computational efficiency and storage cost, and better facilitates the application of LPDM-based flux inversion systems with dense observing systems. To conduct kilometer-scale emission inversions using one day of observations made at the 40 BEACO<sub>2</sub>N sites in the SF Bay Area (approx. 650 observations per day), it takes the full-physics STILT model about 640 core-hours to generate the required footprints. The generation of each footprint prediction takes  $\sim 1$  s on a 32-core compute node, which can be further reduced to 0.08 s on an NVIDIA A2 graphics processing unit (GPU). Only 6 minutes are required for FootNet on an A2 GPU node to generate the required footprints for one day of BEACO<sub>2</sub>N measurements. The storage requirement also makes it impractical to use full-physics models in high-resolution flux inversions with dense observations. Hourly footprints for one week of BEACO<sub>2</sub>N measurements would require 4-terabyte storage space for future re-use. With FootNet, footprints could be generated in near real-time and there is no need to store the computed footprints.

Figure 5 shows the ranking of variable importance for FootNet calculated using the PaP method on 1000 randomly selected data samples. Overall, the most important meteorological variables are the 10-meter wind speeds, which lead to a 0.2~0.3 decrease in correlation and the IoU drops by 0.1~0.2 after being permuted. Permuting Gaussian plumes degrades the correlation and the IoU of FootNet predictions by 0.1 and 0.03, respectively. We find less sensitivity of FootNet predictions to surface pressure and planetary boundary layer height than other input variables. This is because we only have training data from two locations in the current version of the model, and these two meteorological fields show much less variability than the wind fields in the training data set. We still include surface pressure and PBL height as input variables because they are essential information for the generation of measurement footprints. We expect to see greater importance for surface pressure and PBL height for a general version of FootNet trained using footprints from more locations in the future. Figure 5 also shows that input variables from  $t_0$ -6h have consistently greater importance than  $t_0$ .

The PaP method only provides a rough estimate of variable importance, and the inter-correlation between input variables can lead to an inflation of the feature importance (Hooker et al., 2021). Nevertheless, the estimated variable importance for

FootNet is in alignment with with our understanding about the calculation of footprints in a full-physics model, which relies  
190 on the advection of particles driven by precomputed wind fields. The Gaussian plume is also identified as highly important,  
because it is the only input field providing information about the location of receptors.

## 4 Conclusions

We described the development of a machine learning-based emulator of surface measurement footprints, FootNet. The footprint  
emulator can be used to improve the computational efficiency of estimating high-resolution GHG fluxes using measurements  
195 made by dense observing systems. The FootNet model was trained and evaluated using footprints simulated by the STILT  
full-physics model for the SF Bay Area and the Barnett Shale region. We showed the convergence of FootNet predictions to  
the STILT truth as the training iterates. The overall correlation between FootNet predictions and the STILT truth in the test data  
set reaches 0.58 after full convergence. The emulator well predicts both the extents and magnitudes of footprints with a high  
fidelity. We estimated importance of input variables using the PaP method to improve the interpretability of the FootNet model.  
200 We found 10-meter wind speeds and Gaussian plumes have the greatest importance for the emulation of footprints. Emulation  
of footprints using FootNet brings co-benefits for computationally efficient and reducing storage cost, which makes it feasible  
to deliver high-resolution estimates of GHG fluxes in near real-time using proliferated dense observing systems in the future.

Due to the computational cost required by the generation of high-resolution footprints, we only included footprints generated  
from previous studies for the two locations in training version 1.0 of FootNet. We are actively generating new footprints at 1  
205 km from a broader region to further improve the emulator's performance, especially in regions with different meteorological  
conditions from the two locations used in this study (~~?~~[\(Dadheech et al., 2024\)](#)). Generalizing this source-receptor emulator to  
other regions is being tackled in the next version of FootNet.

*Code and data availability.* We use the full-physics Stochastic Time-Inverted Lagrangian Transport Model (STILT) to simulation footprints  
for the training of FootNet. The STILT model could be accessed from <https://uataq.github.io/stilt/> (Fasoli et al., 2018). Footprints simulated  
210 by the STILT model are available through Turner et al. (2018) and Turner et al. (2020). Examples of the footprints used in the train-  
ing process could be downloaded from <https://zenodo.org/records/12803617>, <https://zenodo.org/records/12803736>, and <https://zenodo.org/records/12803855>. The meteorological variables are from the High-Resolution Rapid Refresh (HRRR) data product, which is available at  
<https://rapidrefresh.noaa.gov/hrrr/> (Dowell et al., 2022; James et al., 2022). The repository of the code used in the manuscript is publicly  
available at <https://zenodo.org/records/12752655>.

215 *Author contributions.* T.L.H., N.D., and A.J.T. designed the research study; T.L.H. and N.D. built and trained the model; T.L.H. and N.D.  
performed research and analyzed results; T.L.H., N.D., T.M.T. and A.J.T. contributed to revising and editing the manuscript.

*Competing interests.* The authors declare no conflict of interest.

*Acknowledgements.* This work is supported by a NASA Early Career Faculty Grant (80NSSC21K1808) to A.J.T. and NASA FINESST Grant (80NSSC22K1557) to N.D. We acknowledge funding from Environmental Defense Fund, whose work is supported by gifts from  
220 Signe Ostby, Scott Cook and Valhalla Foundation. This research received support through Schmidt Sciences, LLC.

## References

- Baker, D. F., Doney, S. C., and Schimel, D. S.: Variational data assimilation for atmospheric CO<sub>2</sub>, *Tellus B: Chemical and Physical Meteorology*, 58, 359–365, <https://doi.org/10.1111/j.1600-0889.2006.00218.x>, 2006.
- Benjamin, S. G., Weygandt, S. S., Brown, J. M., Hu, M., Alexander, C. R., Smirnova, T. G., Olson, J. B., James, E. P., Dowell, D. C., Grell,  
225 G. A., Lin, H., Peckham, S. E., Smith, T. L., Moninger, W. R., Kenyon, J. S., and Manikin, G. S.: A North American Hourly Assimilation and Model Forecast Cycle: The Rapid Refresh, *Monthly Weather Review*, 144, 1669 – 1694, <https://doi.org/https://doi.org/10.1175/MWR-D-15-0242.1>, 2016.
- Dadheech, N., He, T.-L., and Turner, A. J.: High-resolution greenhouse gas flux inversions using a machine learning surrogate model for atmospheric transport, *EGUsphere*, 2024, 1–21, <https://doi.org/10.5194/egusphere-2024-2918>, 2024.
- 230 Dobbins, R.: Atmospheric Motion and Air Pollution: An Introduction for Students of Engineering and Science, A Wiley-interscience publication, Wiley, ISBN 9780471216759, <https://books.google.com/books?id=kDhSAAAAMAAJ>, 1979.
- Dowell, D. C., Alexander, C. R., James, E. P., Weygandt, S. S., Benjamin, S. G., Manikin, G. S., Blake, B. T., Brown, J. M., Olson, J. B., Hu, M., Smirnova, T. G., Ladwig, T., Kenyon, J. S., Ahmadov, R., Turner, D. D., Duda, J. D., and Alcott, T. I.: The High-Resolution Rapid Refresh (HRRR): An Hourly Updating Convection-Allowing Forecast Model. Part I: Motivation and System Description, *Weather and*  
235 *Forecasting*, 37, 1371 – 1395, <https://doi.org/https://doi.org/10.1175/WAF-D-21-0151.1>, 2022.
- Fasoli, B., Lin, J. C., Bowling, D. R., Mitchell, L., and Mendoza, D.: Simulating atmospheric tracer concentrations for spatially distributed receptors: updates to the Stochastic Time-Inverted Lagrangian Transport model’s R interface (STILT-R version 2), *Geoscientific Model Development*, 11, 2813–2824, <https://doi.org/10.5194/gmd-11-2813-2018>, 2018.
- Feng, L., Palmer, P. I., Bösch, H., and Dance, S.: Estimating surface CO<sub>2</sub> fluxes from space-borne CO<sub>2</sub> dry air mole fraction observations  
240 using an ensemble Kalman Filter, *Atmospheric Chemistry and Physics*, 9, 2619–2633, <https://doi.org/10.5194/acp-9-2619-2009>, 2009.
- Fillola, E., Santos-Rodriguez, R., Manning, A., O’Doherty, S., and Rigby, M.: A machine learning emulator for Lagrangian particle dispersion model footprints: a case study using NAME, *Geoscientific Model Development*, 16, 1997–2009, [https://doi.org/10.5194/gmd-16-1997-](https://doi.org/10.5194/gmd-16-1997-2023)  
2023, 2023.
- Fisher, A., Rudin, C., and Dominici, F.: All Models are Wrong, but Many are Useful: Learning a Variable’s Importance by Studying an Entire  
245 Class of Prediction Models Simultaneously, *Journal of machine learning research : JMLR*, 20, 2019.
- Ghorbanzadeh, O., Crivellari, A., Ghamisi, P., Shahabi, H., and Blaschke, T.: A comprehensive transferability evaluation of U-Net and ResU-Net for landslide detection from Sentinel-2 data (case study areas from Taiwan, China, and Japan), *Scientific Reports*, 11, 14 629, <https://doi.org/10.1038/s41598-021-94190-9>, 2021.
- Goodfellow, I., Bengio, Y., and Courville, A.: *Deep Learning*, MIT Press, <http://www.deeplearningbook.org>, 2016.
- 250 He, T.-L., Jones, D. B. A., Miyazaki, K., Huang, B., Liu, Y., Jiang, Z., White, E. C., Worden, H. M., and Worden, J. R.: Deep Learning to Evaluate US NO<sub>x</sub> Emissions Using Surface Ozone Predictions, *Journal of Geophysical Research: Atmospheres*, 127, e2021JD035 597, <https://doi.org/https://doi.org/10.1029/2021JD035597>, e2021JD035597 2021JD035597, 2022a.
- He, T.-L., Jones, D. B. A., Miyazaki, K., Bowman, K. W., Jiang, Z., Chen, X., Li, R., Zhang, Y., and Li, K.: Inverse modelling of Chinese NO<sub>x</sub> emissions using deep learning: integrating in situ observations with a satellite-based chemical reanalysis, *Atmospheric Chemistry*  
255 *and Physics*, 22, 14 059–14 074, <https://doi.org/10.5194/acp-22-14059-2022>, 2022b.
- He, T.-L., Boyd, R. J., Varon, D. J., and Turner, A. J.: Increased methane emissions from oil and gas following the Soviet Union’s collapse, *Proceedings of the National Academy of Sciences*, 121, e2314600 121, <https://doi.org/10.1073/pnas.2314600121>, 2024.

- Henze, D. K., Hakami, A., and Seinfeld, J. H.: Development of the adjoint of GEOS-Chem, *Atmospheric Chemistry and Physics*, 7, 2413–2433, <https://doi.org/10.5194/acp-7-2413-2007>, 2007.
- 260 Hooker, G., Mentch, L., and Zhou, S.: Unrestricted Permutation forces Extrapolation: Variable Importance Requires at least One More Model, or There Is No Free Variable Importance, 2021.
- Houtekamer, P. L. and Mitchell, H. L.: A Sequential Ensemble Kalman Filter for Atmospheric Data Assimilation, *Monthly Weather Review*, 129, 123 – 137, [https://doi.org/10.1175/1520-0493\(2001\)129<0123:ASEKFF>2.0.CO;2](https://doi.org/10.1175/1520-0493(2001)129<0123:ASEKFF>2.0.CO;2), 2001.
- IPCC: Global Warming of 1.5°C: IPCC Special Report on Impacts of Global Warming of 1.5°C above Pre-industrial Levels in Context of
- 265 Strengthening Response to Climate Change, Sustainable Development, and Efforts to Eradicate Poverty, Cambridge University Press, <https://doi.org/10.1017/9781009157940>, 2022.
- James, E. P., Alexander, C. R., Dowell, D. C., Weygandt, S. S., Benjamin, S. G., Manikin, G. S., Brown, J. M., Olson, J. B., Hu, M., Smirnova, T. G., Ladwig, T., Kenyon, J. S., and Turner, D. D.: The High-Resolution Rapid Refresh (HRRR): An Hourly Updating Convection-Allowing Forecast Model. Part II: Forecast Performance, *Weather and Forecasting*, 37, 1397 – 1417,
- 270 <https://doi.org/https://doi.org/10.1175/WAF-D-21-0130.1>, 2022.
- Jiang, Z., Worden, J. R., Worden, H., Deeter, M., Jones, D. B. A., Arellano, A. F., and Henze, D. K.: A 15-year record of CO emissions constrained by MOPITT CO observations, *Atmospheric Chemistry and Physics*, 17, 4565–4583, [https://doi.org/10.5194/acp-17-4565-](https://doi.org/10.5194/acp-17-4565-2017)2017, 2017.
- Jones, A., Thomson, D., Hort, M., and Devenish, B.: The U.K. Met Office’s Next-Generation Atmospheric Dispersion Model, NAME III,
- 275 in: *Air Pollution Modeling and Its Application XVII*, edited by Borrego, C. and Norman, A.-L., pp. 580–589, Springer US, Boston, MA, ISBN 978-0-387-68854-1, 2007a.
- Jones, A., Thomson, D., Hort, M., and Devenish, B.: The U.K. Met Office’s Next-Generation Atmospheric Dispersion Model, NAME III,
- in: *Air Pollution Modeling and Its Application XVII*, edited by Borrego, C. and Norman, A.-L., pp. 580–589, Springer US, Boston, MA, ISBN 978-0-387-68854-1, 2007b.
- 280 Kang, J.-S., Kalnay, E., Liu, J., Fung, I., Miyoshi, T., and Ide, K.: “Variable localization” in an ensemble Kalman filter: Application to the carbon cycle data assimilation, *Journal of Geophysical Research: Atmospheres*, 116, <https://doi.org/https://doi.org/10.1029/2010JD014673>, 2011.
- Karion, A., Callahan, W., Stock, M., Prinzivalli, S., Verhulst, K. R., Kim, J., Salameh, P. K., Lopez-Coto, I., and Whetstone, J.: Greenhouse gas observations from the Northeast Corridor tower network, *Earth System Science Data*, 12, 699–717, [https://doi.org/10.5194/essd-12-](https://doi.org/10.5194/essd-12-699-2020)
- 285 699-2020, 2020.
- Lauvaux, T., Gurney, K. R., Miles, N. L., Davis, K. J., Richardson, S. J., Deng, A., Nathan, B. J., Oda, T., Wang, J. A., Hutyra, L., and Turnbull, J.: Policy-Relevant Assessment of Urban CO<sub>2</sub> Emissions, *Environmental Science & Technology*, 54, 10237–10245, <https://doi.org/10.1021/acs.est.0c00343>, PMID: 32806908, 2020.
- Lin, J. C., Gerbig, C., Wofsy, S. C., Andrews, A. E., Daube, B. C., Davis, K. J., and Grainger, C. A.: A near-field tool for simulating the up-
- 290 stream influence of atmospheric observations: The Stochastic Time-Inverted Lagrangian Transport (STILT) model, *Journal of Geophysical Research: Atmospheres*, 108, <https://doi.org/https://doi.org/10.1029/2002JD003161>, 2003.
- Lin, J. C., Gerbig, C., Wofsy, S. C., Andrews, A. E., Daube, B. C., Grainger, C. A., Stephens, B. B., Bakwin, P. S., and Hollinger, D. Y.: Measuring fluxes of trace gases at regional scales by Lagrangian observations: Application to the CO<sub>2</sub> Budget and Rectification Airborne (COBRA) study, *Journal of Geophysical Research: Atmospheres*, 109, <https://doi.org/https://doi.org/10.1029/2004JD004754>, 2004.

- 295 Lin, J. C., Bares, R., Fasoli, B., Garcia, M., Crosman, E., and Lyman, S.: Declining methane emissions and steady, high leakage rates observed over multiple years in a western US oil/gas production basin, *Scientific Reports*, 11, 22 291, <https://doi.org/10.1038/s41598-021-01721-5>, 2021.
- Mitchell, L. E., Lin, J. C., Bowling, D. R., Pataki, D. E., Strong, C., Schauer, A. J., Bares, R., Bush, S. E., Stephens, B. B., Mendoza, D., Mallia, D., Holland, L., Gurney, K. R., and Ehleringer, J. R.: Long-term urban carbon dioxide observations reveal spatial and  
300 temporal dynamics related to urban characteristics and growth, *Proceedings of the National Academy of Sciences*, 115, 2912–2917, <https://doi.org/10.1073/pnas.1702393115>, 2018.
- Miyazaki, K., Eskes, H., Sudo, K., Boersma, K. F., Bowman, K., and Kanaya, Y.: Decadal changes in global surface NO<sub>x</sub> emissions from multi-constituent satellite data assimilation, *Atmospheric Chemistry and Physics*, 17, 807–837, <https://doi.org/10.5194/acp-17-807-2017>, 2017.
- 305 Miyazaki, K., Bowman, K. W., Yumimoto, K., Walker, T., and Sudo, K.: Evaluation of a multi-model, multi-constituent assimilation framework for tropospheric chemical reanalysis, *Atmospheric Chemistry and Physics*, 20, 931–967, <https://doi.org/10.5194/acp-20-931-2020>, 2020.
- Pisso, I., Sollum, E., Grythe, H., Kristiansen, N. I., Cassiani, M., Eckhardt, S., Arnold, D., Morton, D., Thompson, R. L., Groot Zwaafink, C. D., Evangeliou, N., Sodemann, H., Haimberger, L., Henne, S., Brunner, D., Burkhardt, J. F., Fouilloux, A., Brioude, J., Philipp, A.,  
310 Seibert, P., and Stohl, A.: The Lagrangian particle dispersion model FLEXPART version 10.4, *Geoscientific Model Development*, 12, 4955–4997, <https://doi.org/10.5194/gmd-12-4955-2019>, 2019.
- Qu, Z., Henze, D. K., Worden, H. M., Jiang, Z., Gaubert, B., Theys, N., and Wang, W.: Sector-Based Top-Down Estimates of NO<sub>x</sub>, SO<sub>2</sub>, and CO Emissions in East Asia, *Geophysical Research Letters*, 49, e2021GL096 009, <https://doi.org/https://doi.org/10.1029/2021GL096009>, e2021GL096009 2021GL096009, 2022.
- 315 Ronneberger, O., Fischer, P., and Brox, T.: U-Net: Convolutional Networks for Biomedical Image Segmentation, in: *Medical Image Computing and Computer-Assisted Intervention – MICCAI 2015*, edited by Navab, N., Hornegger, J., Wells, W. M., and Frangi, A. F., *Lecture Notes in Computer Science*, pp. 234–241, Springer International Publishing, Cham, ISBN 978-3-319-24574-4, [https://doi.org/10.1007/978-3-319-24574-4\\_28](https://doi.org/10.1007/978-3-319-24574-4_28), 2015.
- Roten, D., Wu, D., Fasoli, B., Oda, T., and Lin, J. C.: An Interpolation Method to Reduce the Computational Time in the Stochastic Lagrangian Particle Dispersion Modeling of Spatially Dense XCO<sub>2</sub> Retrievals, *Earth and Space Science*, 8, e2020EA001 343, <https://doi.org/https://doi.org/10.1029/2020EA001343>, e2020EA001343 2020EA001343, 2021.
- Shusterman, A. A., Teige, V. E., Turner, A. J., Newman, C., Kim, J., and Cohen, R. C.: The BErkeley Atmospheric CO<sub>2</sub> Observation Network: initial evaluation, *Atmospheric Chemistry and Physics*, 16, 13 449–13 463, <https://doi.org/10.5194/acp-16-13449-2016>, 2016.
- Stein, A. F., Draxler, R. R., Rolph, G. D., Stunder, B. J. B., Cohen, M. D., and Ngan, F.: NOAA’s HYSPLIT Atmospheric Transport and  
325 Dispersion Modeling System, *Bulletin of the American Meteorological Society*, 96, 2059 – 2077, <https://doi.org/10.1175/BAMS-D-14-00110.1>, 2015.
- Stern, A.: *Air Pollution: Volume 1 - Air Pollutants, Their Transformation and Transport*, Environmental sciences, Academic Press, <https://books.google.com/books?id=2qsytAEACAAJ>, 1976.
- Stohl, A., Forster, C., Eckhardt, S., Spichtinger, N., Huntrieser, H., Heland, J., Schlager, H., Wilhelm, S., Arnold, F., and Cooper, O.: A backward modeling study of intercontinental pollution transport using aircraft measurements, *Journal of Geophysical Research: Atmospheres*,  
330 108, <https://doi.org/https://doi.org/10.1029/2002JD002862>, 2003.

- Stohl, A., Seibert, P., Arduini, J., Eckhardt, S., Fraser, P., Grealley, B. R., Lunder, C., Maione, M., Mühle, J., O'Doherty, S., Prinn, R. G., Reimann, S., Saito, T., Schmidbauer, N., Simmonds, P. G., Vollmer, M. K., Weiss, R. F., and Yokouchi, Y.: An analytical inversion method for determining regional and global emissions of greenhouse gases: Sensitivity studies and application to halocarbons, *Atmospheric Chemistry and Physics*, 9, 1597–1620, <https://doi.org/10.5194/acp-9-1597-2009>, 2009.
- Tucker, C., Brandt, M., Hiernaux, P., Kariryaa, A., Rasmussen, K., Small, J., Igel, C., Reiner, F., Melocik, K., Meyer, J., Sinno, S., Romero, E., Glennie, E., Fitts, Y., Morin, A., Pinzon, J., McClain, D., Morin, P., Porter, C., Loeffler, S., Kergoat, L., Issoufou, B.-A., Savadogo, P., Wigneron, J.-P., Poulter, B., Ciais, P., Kaufmann, R., Myneni, R., Saatchi, S., and Fensholt, R.: Sub-continental-scale carbon stocks of individual trees in African drylands, *Nature*, 615, 80–86, <https://doi.org/10.1038/s41586-022-05653-6>, 2023.
- Turner, A. J., Jacob, D. J., Benmergui, J., Brandman, J., White, L., and Randles, C. A.: Assessing the capability of different satellite observing configurations to resolve the distribution of methane emissions at kilometer scales, *Atmospheric Chemistry and Physics*, 18, 8265–8278, <https://doi.org/10.5194/acp-18-8265-2018>, 2018.
- Turner, A. J., Kim, J., Fitzmaurice, H., Newman, C., Worthington, K., Chan, K., Wooldridge, P. J., Köehler, P., Frankenberg, C., and Cohen, R. C.: Observed Impacts of COVID-19 on Urban CO<sub>2</sub> Emissions, *Geophysical Research Letters*, 47, e2020GL090037, <https://doi.org/https://doi.org/10.1029/2020GL090037>, e2020GL090037 10.1029/2020GL090037, 2020.
- United Nations Publications: World Urbanization Prospects: The 2018 Revision, UN, ISBN 9789211483192, <https://books.google.com/books?id=Kp9AygEACAAJ>, 2019.
- Veefkind, J., Aben, I., McMullan, K., Förster, H., de Vries, J., Otter, G., Claas, J., Eskes, H., de Haan, J., Kleipool, Q., van Weele, M., Hasekamp, O., Hoogeveen, R., Landgraf, J., Snel, R., Tol, P., Ingmann, P., Voors, R., Kruizinga, B., Vink, R., Visser, H., and Levelt, P.: TROPOMI on the ESA Sentinel-5 Precursor: A GMES mission for global observations of the atmospheric composition for climate, air quality and ozone layer applications, *Remote Sensing of Environment*, 120, 70–83, <https://doi.org/https://doi.org/10.1016/j.rse.2011.09.027>, the Sentinel Missions - New Opportunities for Science, 2012.
- White, E. D., Rigby, M., Lunt, M. F., Smallman, T. L., Comyn-Platt, E., Manning, A. J., Ganesan, A. L., O'Doherty, S., Stavert, A. R., Stanley, K., Williams, M., Levy, P., Ramonet, M., Forster, G. L., Manning, A. C., and Palmer, P. I.: Quantifying the UK's carbon dioxide flux: an atmospheric inverse modelling approach using a regional measurement network, *Atmospheric Chemistry and Physics*, 19, 4345–4365, <https://doi.org/10.5194/acp-19-4345-2019>, 2019.
- Zannetti, P.: Gaussian Models, pp. 141–183, Springer US, Boston, MA, ISBN 978-1-4757-4465-1, [https://doi.org/10.1007/978-1-4757-4465-1\\_7](https://doi.org/10.1007/978-1-4757-4465-1_7), 1990.
- Zemskova, V. E., He, T.-L., Wan, Z., and Grisouard, N.: A deep-learning estimate of the decadal trends in the Southern Ocean carbon storage, *Nature Communications*, 13, 4056, <https://doi.org/10.1038/s41467-022-31560-5>, 2022.

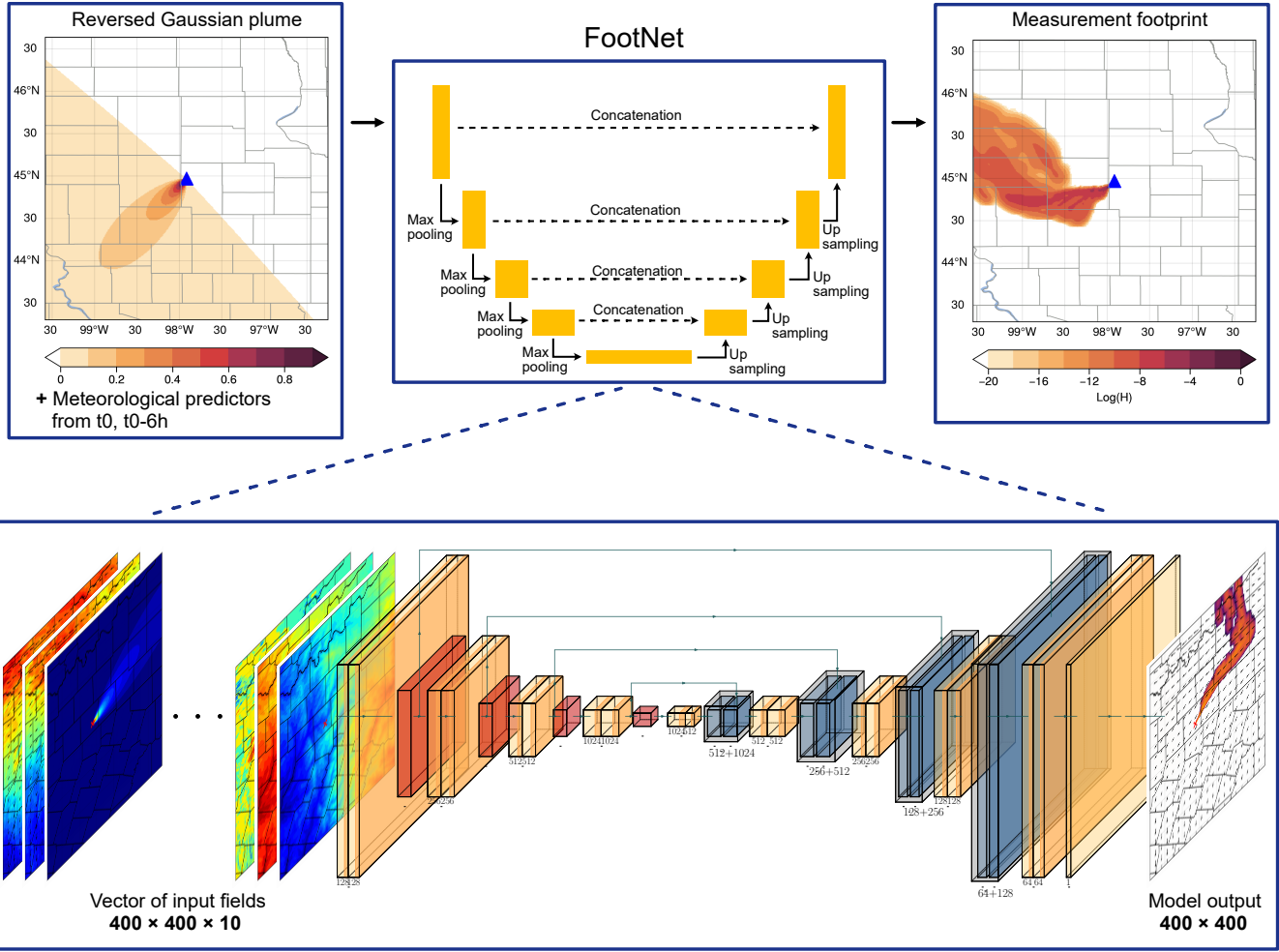


**Figure 1.** Top row shows the schematic diagram of the FootNet model. Detailed structure of FootNet is shown at the bottom. The orange boxes indicate  $3 \times 3$  convolutional layers. The red boxes represent  $2 \times 2$  max-pooling layers. The light blue boxes are  $2 \times 2$  transposed convolutional layers. The dark blue boxes represent the latent vectors concatenated from previous layers (shown as parallel arrows on top).

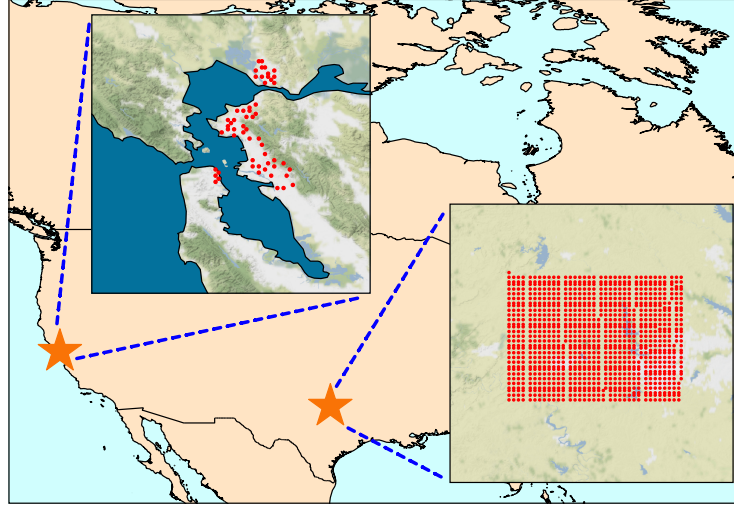


**Figure 2.** Location of receptors for simulations of measurement footprints using the STILT model. Receptors in the SF Bay Area are located at sites in the BEACO<sub>2</sub>N network (Shusterman et al., 2016). Receptors in the Barnett Shale region are at locations used in Turner et al. (2018). Map tiles are from © Stamen Design, under a Creative Commons Attribution (CC BY 3.0) license.

**Table 1.** Information about input variables of FootNet.

Variable (Unit)	Description	Time steps	Scaling factor
Gaussian plume	Idealized plumes calculated using reversed winds	$t_0, t_0-6h$	1
U10M (m/s)	10-meter U-component of wind	$t_0, t_0-6h$	10
V10M (m/s)	10-meter V-component of wind	$t_0, t_0-6h$	10
PBLH (m)	PBL height	$t_0, t_0-6h$	1e-3
PRSS (hPa)	Surface pressure	$t_0, t_0-6h$	1e-3

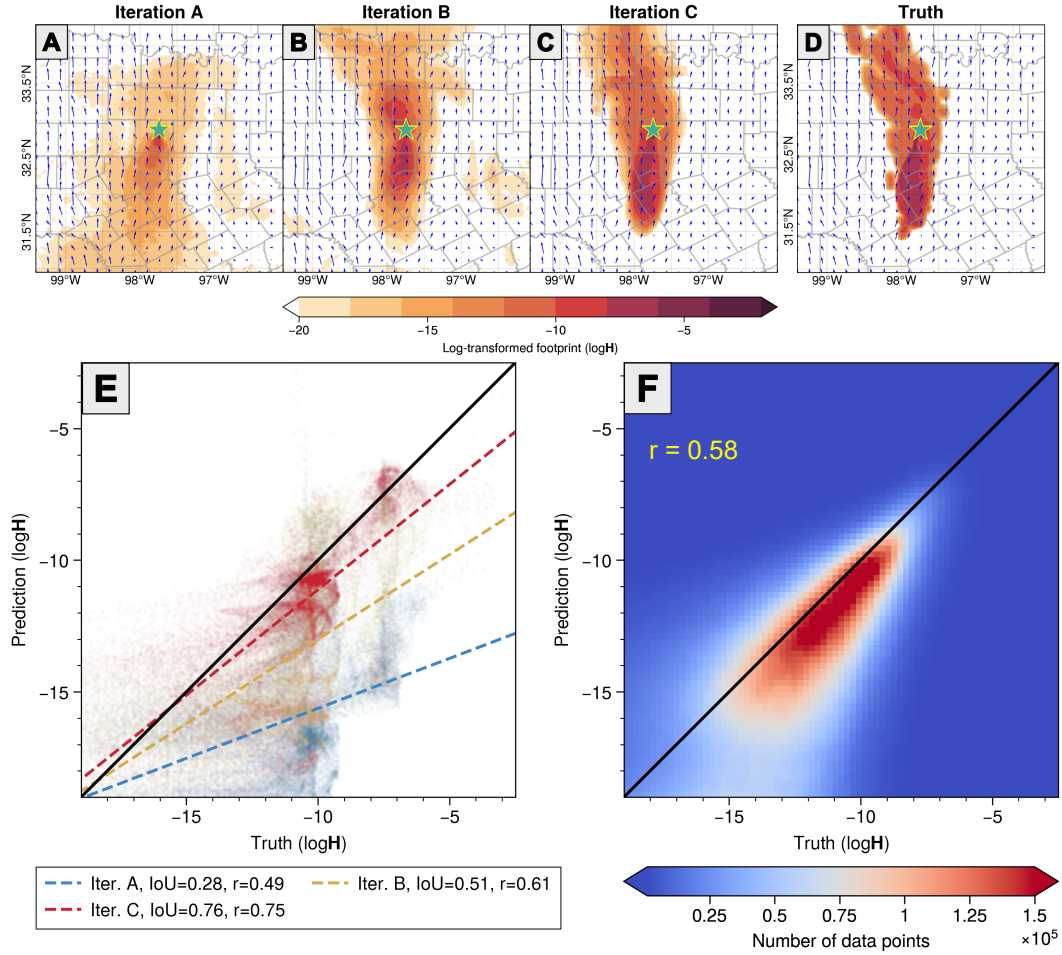


**Figure 3.** Convergence of the training process and evaluation of the model performance on the independent test data set. Footprints are transformed using natural logarithm. The unit of footprints is ppb / (nmol m<sup>-2</sup> s<sup>-1</sup>) before the transformation. (A-C) FootNet predictions from three stages in the training process, corresponding to the truth in (D). The blue arrows represent wind vectors, and the green stars show the location of the receptors. (E) Comparison between footprints simulated by STILT and FootNet predictions in (A-C). (F) Two-dimensional histogram of all natural log-transformed footprint (logH) values simulated by STILT and the corresponding predictions made by FootNet from the test data set.

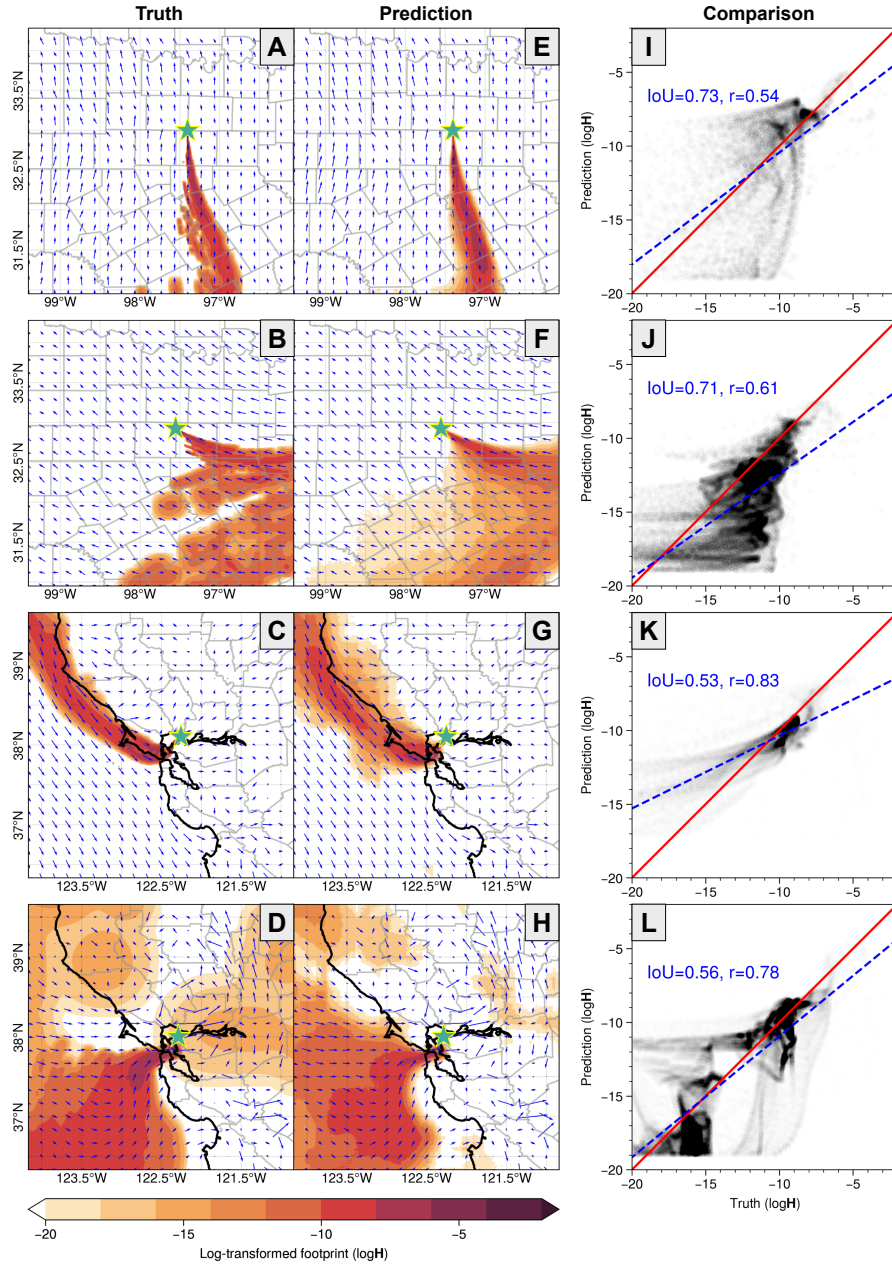


**Figure 4.** Evaluation of individual FootNet predictions from the test data set. Footprints are transformed using natural logarithm. The unit of footprints is  $\text{ppb} / (\text{nmol m}^{-2} \text{s}^{-1})$  before the transformation. (A-D) Footprints simulated by the full-physics STILT model for the Barnett Shale region and the SF Bay Area. (E-H) Footprint predictions made by FootNet corresponding to (A-D). The blue arrows represent wind vectors, and the green stars show the location of the receptors. (I-L) Comparison and correlation between the truth and predictions for the four examples.

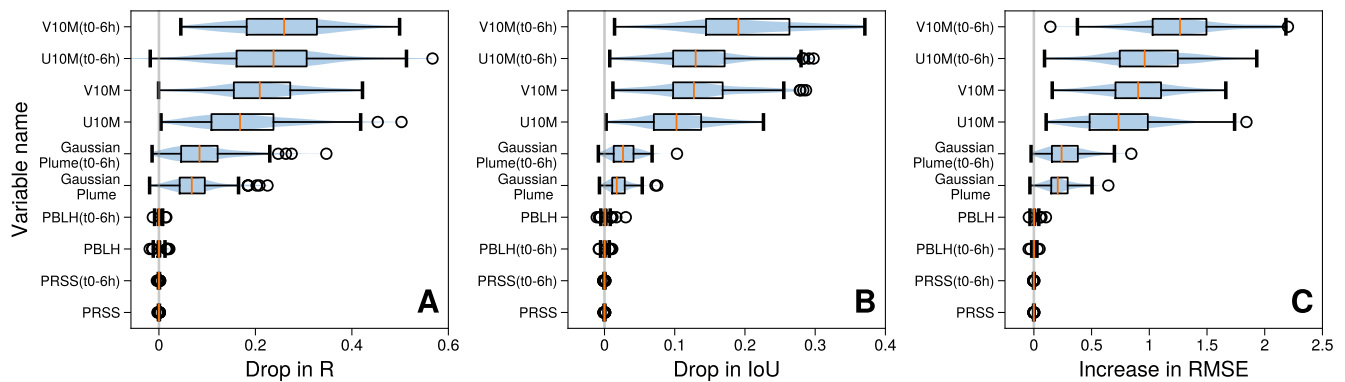


**Figure 5.** Rankings of variable importance estimated using the permute-and-predict (PaP) method on 1000 data samples. (A-C) Variable importance shown as drop in correlation, drop in the IoU, and increase in the RMSE after permuting the 10 input variables. Orange lines show the medians. Boxes indicate ranges from the first quartiles to the third quartiles. Whiskers are the 1.5 interquartile ranges (IQRs) from the boxes. Circles are outliers.